JOURNAL OF THERMOPHYSICS AND HEAT TRANSFER
Vol. 19, No. 4, October–December 2005

Coupling Heat Transfer and Fluid Flow Solvers for Multidisciplinary Simulations

Q. Y. Liu,* E. A. Luke,† and P. Cinnella‡
Mississippi State University, Mississippi State, Mississippi 39762

The feasibility of multidisciplinary simulations for realistic geometries involving detailed physical models is demonstrated. Specifically, a three-dimensional chemically reacting fluid flow solver is coupled with a solid-phase heat transfer solver that includes cooling channels. Both fluid- and solid-phase models employ the integral, conservative form of the governing equations and are discretized by means of two finite volume numerical schemes. To keep the heat flux consistent, a special algorithm is developed at the interface between the solid and fluid regions. Physical and thermal properties of the solid materials can be temperature dependent, and different materials can be used in different parts of the domains due to a multiblock gridding strategy. The cooling channel model is developed by using conservation laws of mass, momentum, and energy, taking into account the effects of heat transfer and friction. The coupling of the models (solid and fluid, solid and cooling channels) is detailed. A hot-air nozzle test case is examined, and the simulated results are validated by means of available experimental data. Finally, a more complex case is simulated, involving the water-cooled nozzle of a rocket-based combined cycle thruster. This case employs all three models, fully coupled. The calculated temperatures in the nozzle wall and at the cooling channel outlet are compared with experimental data and are in reasonably close agreement.

Nomenclature

A	=	area
c_v, c_p	=	specific heats (per unit mass)
D	=	diameter or hydraulic diameter
E	=	solid-phase energy (per unit volume)
e	=	roughness
$\boldsymbol{F}_i$, $\boldsymbol{F}_v$	=	inviscid and viscous flux vectors
f	=	friction factor
G	=	thermal source (per unit volume)
g	=	gravity constant
h	=	enthalpy (per unit mass)
h_f	=	local heat transfer coefficient
k	=	thermal conductivity
L	=	length of cooling cell
$\dot{m}$	=	mass flow rate
Nu	=	Nusselt number
$\boldsymbol{n}$	=	unit vector, normal to the surface A
Pr	=	Prandtl number
p	=	pressure
Q	=	heat per unit mass
$\boldsymbol{Q}$	=	vector of conservative variables
$\boldsymbol{q}$	=	conductive heat flux vector
R	=	numerical residual
Re	=	Reynolds number
$\boldsymbol{r}$	=	position vector
T	=	temperature
t	=	time
V	=	velocity magnitude; volume
v	=	specific volume
$\dot{W}$	=	chemistry source term
x	=	position coordinate
y^+	=	nondimensional normal distance from solid wall (viscous flow)
z	=	elevation
μ	=	dynamic viscosity
ρ	=	density
Ω	=	control volume, bounded by the control surface $\partial\Omega$

Subscripts

av	=	average value
c	=	cell
cool	=	cooling channel
fc	=	face
ref	=	reference value
wall	=	cooling channel wall
1	=	inlet
2	=	outlet

Presented as Paper 2004-0996 at the AIAA 42nd Aerospace Sciences Meeting and Exhibit, Reno, NV, 5–8 January 2004; received 19 September 2004; revision received 25 January 2005; accepted for publication 25 January 2005.

*Postdoctoral Associate, Center for Advanced Vehicular Systems, 200 Research Park; liuqy@cavs.msstate.edu.

†Assistant Professor, Department of Computer Science and Engineering, 300 Butler; luke@cse.msstate.edu. Member AIAA.

‡Professor, Department of Aerospace Engineering, 330 Walker; cinnella@ae.msstate.edu. Senior Member of AIAA.

I. Introduction

THE goal of heat transfer studies is the accurate prediction of temperature and heat flux distribution in space, and possibly time, in a material and on its boundaries. The temperature field is important when one has to consider thermal stresses and material properties, which are the key elements for the optimal design of thermal structures, or the development of new composite materials. Numerical modeling, because of its flexibility, can deal with irregular boundaries and complicated physical circumstances, and has received considerable attention as a tool for finding solutions to practical engineering problems. However, the boundary conditions to be imposed at the surfaces to determine the heat transfer to a solid body may not be specified easily for a practical situation. One case in point is the thermally convective wall (heating or cooling), where the heat transfer coefficient or heat flux should be obtained from a solution of the coupled solid–fluid problem. Therefore, numerical models have to be developed considering both solid and fluid regions, and the solution of the coupled problem can then be recovered.

The literature on thermally convective walls is enormous. A few references closely related to the present effort are briefly summarized in the following text. Shope[1] dealt with the cooling of a nozzle

wall for a supersonic wind tunnel. DeLise and Naraghi[2] solved the compressible boundary-layer equations and evaluated the convective heat transfer rates from high-temperature combustion gases to the converging–diverging nozzle of a liquid-fueled rocket engine. Janus and Newman[3] coupled aerodynamic and thermal effects for an optimization study of turbine airfoil design. Sondak and Dorney[4] investigated coupled unsteady flow and heat conduction for a turbine stage. Webster[5] developed a heat-conduction solver and coupled it with an existing flow solver. He also discussed some issues related to ensuring thermal communication between solid grid blocks. Naraghi[6] developed a rocket thermal evaluation code for regeneratively cooled rocket thrust chambers and nozzles. In this approach, either the CET code can be used for the evaluation of hot-gas properties assuming local chemical equilibrium, or the TDK program can be employed,[7] which is based on finite-rate chemistry. Then the GASP/WASP codes can be used to calculate the coolant flow properties.[8,9] Pal et al.[10] investigated the heat transfer characteristics of a gaseous oxygen (GO_2)/gaseous hydrogen (GH_2) two-dimensional compact rocket thruster, especially in the nozzle region. Thermocouples were buried deep inside the nozzle wall to measure the axial temperature profile. The nozzle was heavily cooled by means of several water channels during the thruster firing. The authors also provided analytical results, using the FDNS code (see Ref. 11) for the fluid simulation, and a one-dimensional heat transfer model based on Bartz's correction[12,13] to calculate the nozzle wall heat flux and temperature from the measured temperature inside the nozzle wall.

In summary, much effort has been focused on the development of individual flow fluid or solid heat transfer models, and some attention has been paid to model coupling. However, the coupling has been typically conducted through explicit boundary conditions, in a loosely coupled fashion. Consequently, there is a strong need for more studies to address the issues of model coupling in various practical applications. The present study is focused on demonstrating that it is possible to obtain accurate simulations of heat transfer and temperature fields in multiphase, complicated geometries of engineering interest. The current work is based on the Loci system,[14–17] which was developed at Mississippi State University. The Loci system is an application framework that seeks to reduce the complexity of assembling large-scale finite difference, finite volume, or finite element applications. It is well known that a significant number of errors in large-scale computational field simulations are caused by incorrect looping structures, improper calling sequences, or incorrect data transfers, especially between various application components. The Loci framework solves these problems by automatically generating the control and data movement operations of an application from component specifications, while keeping data consistent between components. The system connects user applications through data models and computation rules. Detailed information can be found in Ref. 14.

CHEM is a flow solver developed within Loci that includes complex thermodynamic, chemistry, transport, and turbulent models. A finite volume method for three-dimensional generalized grids, a Roe-type flux discretization technique, and explicit or implicit time integration schemes are employed. The successful development of CHEM has demonstrated the flexibility of Loci to deal with multiphysical models.[18] It is now possible to couple heat transfer models to the flow solver and to obtain accurate simulations of heat transfer and temperature fields in both solid and fluid phases. This is the goal of the present study. In particular, two heat transfer models have been coupled with CHEM within the Loci system: The first is a solid heat conduction model, the latter is a quasi-one-dimensional cooling channel model. Some effort was made to develop algorithms for the treatment of the interface, to ensure the consistency of the data at the phase boundaries. The coupling processes, based on the Loci data structure and computation rules, are presented here to demonstrate the flexibility of this system for the seamless integration of multiphysical components.

In the following text, the governing equations for both the fluid and solid phase are summarized. Some details on the numerical discretization of the equations are provided, with emphasis placed on the coupling between the different models. Two realistic engineering applications are studied using CHEM and the newly developed heat transfer models. The first one involves a hot-air nozzle wall, and the computed results are validated by means of available experimental data. The second geometry is more complex, involves the water-cooled nozzle of a rocket-based combined cycle (RBCC) thruster, and requires all three models, fully coupled. The calculated temperatures in the nozzle wall and at the cooling channel outlet compare favorably with the experimental data.

II. Governing Equations

The present study is focused on the two heat transfer models already mentioned and the issues that arise from the coupling with the fluid flow solver. Consequently, in the following text, both fluid- and solid-phase governing equations are briefly presented.

A. Governing Equations for Fluid Phase

A finite volume method is applied to discretize the flow equations. After integration over a computational cell or control volume, the governing equations in vector form can be written as follows:

$$\frac{\mathrm{d}}{\mathrm{d}t}\int_{\Omega_c(t)} \boldsymbol{Q}\,\mathrm{d}V + \int_{\partial\Omega_c(t)} (\boldsymbol{F}_i - \boldsymbol{F}_v)\,\mathrm{d}A = \int_{\Omega_c(t)} \dot{W}\,\mathrm{d}V \tag{1}$$

where $\boldsymbol{Q}$ is the vector of conservative variables. The CHEM code is able to accommodate a vast range of thermophysical models, including mixtures of chemically reacting gases. Several turbulence models have been included and validated,[16] among them the one-equation Spalart–Allmaras model[19] and a family of two-equation models including the baseline (BSL) formulation by Menter.[20] More details on the governing equations and all related thermochemical issues can be found in Ref. 14.

B. Governing Equations for Solid Phase

The basic governing equation for the solid heat conduction model is obtained by applying the principle of conservation of energy to a control volume. In integral form, the final result reads

$$\frac{\mathrm{d}}{\mathrm{d}t}\int_{\Omega_c(t)} E\,\mathrm{d}V + \int_{\partial\Omega_c(t)} \boldsymbol{q}\cdot\boldsymbol{n}\,\mathrm{d}A = \int_{\Omega_c(t)} G\,\mathrm{d}V \tag{2}$$

A relationship between temperature and solid-phase energy can be stated as

$$E = \rho\int_{T_{\mathrm{ref}}}^{T} c_v(\tau)\,\mathrm{d}\tau + E_{\mathrm{ref}} \tag{3}$$

Fourier's law of conduction is applied to compute the local heat flux. For isotropic materials, in which the thermal conductivity k is the same in all directions, the conductive heat flux is written as

$$\boldsymbol{q} = -k\nabla T \tag{4}$$

Both c_v and k can depend on temperature and location.

C. Governing Equations for Cooling Channel Flow

The governing equations for a cooling channel flow are developed by using conservation laws for mass, momentum, and energy. The main effects of heat transfer and friction are taken into account. Moreover, assuming that flow parameters change mostly in the flow direction (streamwise), transverse variations are ignored. The resulting quasi-one-dimensional governing equations for a cooling channel flow can be written as follows:

$$\rho_1 V_1 A_1 = \rho_2 V_2 A_2$$

$$\frac{p_1}{\rho_{\mathrm{av}}} + \frac{V_1^2}{2} + gz_1 = \frac{p_2}{\rho_{\mathrm{av}}} + \frac{V_2^2}{2} + gz_2 + \int_1^2 \frac{V^2}{2}\frac{f}{D}\,\mathrm{d}x$$

$$\Delta Q + h_1 + \frac{V_1^2}{2} + gz_1 = h_2 + \frac{V_2^2}{2} + gz_2 \tag{5}$$

where subscripts 1 and 2 represent the inlet and outlet sections of a cooling channel segment, $\rho_{av} = (\rho_1 + \rho_2)/2$, and ΔQ is the heat lost by the solid matrix and gained by the cooling fluid.

For fully developed laminar pipe flow, the Fanning friction factor is calculated (see Ref. 21) as

$$f = 16/Re, \qquad \text{for} \qquad Re \le 2300, \qquad Re = \rho V D/\mu \tag{6}$$

For fully developed turbulent pipe flow, the Colebrook equation[22] can be used to calculate the friction factor. Chen[23] approximated it by an explicit formula,

$$\frac{1}{2\sqrt{f}} = -2.0 \log \left\{ \frac{e}{3.7065D} - \frac{5.0452}{Re} \log \left[\frac{1}{2.8257} \left(\frac{e}{D} \right)^{1.1098} + \frac{5.8506}{Re^{0.8981}} \right] \right\} \tag{7}$$

which is valid for $2300 \le Re \le 10^8$ and $e/D \le 0.05$. The thermodynamic parameters are calculated based on the standard released by the International Association for Properties of Water and Steam (IAPWS).[24] The formulation is based on the Helmholtz function (see Ref. 8) and its partial derivatives. In the present study, values of pressure and enthalpy are provided to the thermodynamic black box, and values for density and temperature are recovered. Additionally, interpolating equations are recommended by IAPWS to calculate viscosity and thermal conductivity.[25,26]

Note that the present model can accommodate phase changes. When this happens, a mixture model is applied, resulting in a single-fluid approach. The assumption is that the two phases are interpenetrating and moving at the same velocity, and vapor quality is limited to a small value. Some examples of mildy two-phase flow in cooling channels are shown in Ref. 27. However, the application presented in this study involves a liquid coolant.

III. Numerical Method

As already mentioned, the two heat transfer models introduced earlier are implemented within the Loci system and coupled with the CHEM flow solver. Loci allows each physical model to be simulated by a numerical method that is best suited for the accuracy and robustness of the overall procedure. In this study, a finite volume method is employed for the solid heat conduction model, and a steady-state integral method is employed for the cooling channel model. Incidentally, the flow solver CHEM is an application template built on Loci, and some of its parts can be reused to develop new models. On the other hand, new rules are required for the interface between different physical models. Loci is designed to generate control and data movement operations automatically, to facilitate the coupling of multidisciplinary models.[14] In the following text, numerical schemes for the solid heat conduction and cooling channel models are given, and the coupling process with the flow solver is presented.

A. Solid Heat Conduction

Starting from Eq. (2), written for a small control volume, the energy integral can be approximated as

$$\int_{\Omega_c(t)} E \, \mathrm{d}V \approx E_c(t) \int_{\Omega_c(t)} \mathrm{d}V = E_c(t) V_c(t) \tag{8}$$

where $E_c(t)$ is the value of E at the cell centroid, $V_c(t)$ is the control volume, and subscript c represents a generic cell. A similar result applies to the thermal source integral.

The surface integral representing the heat flux is discretized by summing contributions at each face of the cell. Here, a generalized grid can be used. Generalized grids are discretizations composed of arbitrary polyhedra, including tetrahedra, prisms, pyramids, and hexahedra.[28] The face temperature gradient is mapped from the cell center temperature gradient, which is constructed by a linear least-squares fit method. (See Luke et al.[18] for details.) In summary, the numerical surface integral is approximated as

$$\int_{\partial\Omega_c(t)} \boldsymbol{q} \cdot \boldsymbol{n} \, \mathrm{d}A = \sum_{fc=1}^{m} \int_{\partial\Omega_{c,fc}(t)} q_{fc} \, \mathrm{d}A \approx \sum_{fc=1}^{m} A_{fc}(t) q_{fc} \tag{9}$$

where q_{fc} is the face heat flux, A_{fc} is the area of the face, and m is the number of faces for the given cell.

At this point, Eq. (2) can be numerically approximated by the equation

$$\frac{\mathrm{d}}{\mathrm{d}t}[V_c(t) E_c(t)] + \sum_{fc=1}^{m} A_{fc}(t) q_{fc} = V_c(t) G_c(t) \tag{10}$$

If the mesh is fixed, then an ordinary differential equation is derived, which reads

$$\frac{\mathrm{d}E_c(t)}{\mathrm{d}t} = R[E_c(t), t] = G_c(t) - \frac{1}{V_c} \sum_{fc=1}^{m} A_{fc} q_{fc} \tag{11}$$

Equation (11) must be satisfied simultaneously for all cells as time changes. Therefore, a global system of ordinary differential equation results and is given by the following equation, removing the subscript c at this juncture:

$$\frac{\mathrm{d}E(t)}{\mathrm{d}t} = R[E(t), t] \tag{12}$$

where $E(t)$ represents the values at all cells at time t.

The implicit time integration scheme for Eq. (12) employs a two-parameter family of algorithms and is given as follows:

$$[(1+\varphi)\Delta E^n - \varphi \Delta E^{n-1}]/\Delta t = (1-\theta) R^n(E^n) + \theta R^{n+1}(E^{n+1}) \tag{13}$$

where n stands for the current time level and $\Delta E^n = E^{n+1} - E^n$. In this scheme, φ and θ form a two-parameter family of algorithms. For example, setting $\theta = 1$, $\varphi = 0$ gives the implicit backward Euler scheme typically used for steady-state simulations, whereas a second-order-accurate three-point backward scheme ($\theta = 1$, $\varphi = \frac{1}{2}$) can be used for time-accurate simulations.

Equation (13) is a nonlinear system of equations for the variable E^{n+1}, and can be solved by Newton iterative methods, as follows:

$$L'(E^{n+1,p})(E^{n+1,p+1} - E^{n+1,p}) = -L(E^{n+1,p}) \tag{14}$$

where the superscript p denotes the Newton itartion counter and

$$L(E^{n+1}) = E^{n+1} - E^n - [\Delta t/(1+\varphi)][(1-\theta)R^n(E^n) + \theta R^{n+1}(E^{n+1})] - [\varphi/(1+\varphi)](E^n - E^{n-1}) = 0 \tag{15}$$

The Jacobian L' in Eq. (14) is given as

$$L'(E^{n+1}) = I - \Delta t \frac{\theta}{1+\varphi} \frac{\partial}{\partial E}[R^{n+1}(E)] = I - \Delta t \frac{\theta}{1+\varphi} \left[\frac{\partial G}{\partial E} - \frac{1}{V} \sum_{fc=1}^{m} A_{fc}^{n+1} \frac{\partial q_{fc}(E)}{\partial E} \right] \tag{16}$$

The Newton iteration is initialized using the preceding time-step value ($E^{n+1,p=0} = E^n$). The Jacobian matrices in Eq. (16) can be evaluated analytically or numerically. More details can be found in Ref. 27. Equation (14) is now linear and can be solved using a Gauss–Seidel iteration method.

B. Coupling Fluid and Solid Models

The flow solver CHEM also employs a finite volume numerical scheme, and has the same three iteration levels: time-step iteration, Newton iteration, and Gauss–Seidel iteration. Consequently, the solid heat conduction model can be fully coupled with the CHEM flow solver into a seamless application within the Loci framework. Here, fully coupled means that the two models are coupled at the

Newton iteration level of the time integrator, as opposed to loosely coupled stand-alone codes. Because of the tight coupling, this new model is appropriate for time-accurate problems if needed. For unsteady time-accurate problems, the same time step is used for flow and solid parts, whereas for steady-state problems, different time steps can be used for each model.

Solid and flow solvers are coupled by keeping the heat flux term consistent at the interface between fluid and solid components. The fluid employs the interface temperature from the solid solver to calculate the heat flux term, whereas the solid employs the interface heat flux to evaluate the temperature in return

$$\begin{array}{c} \nearrow \rightarrow\rightarrow\rightarrow\rightarrow\rightarrow\rightarrow\rightarrow \searrow \\ q_{\text{solid}} \Leftarrow q_{fc} \Leftarrow q_{\text{fluid}} \Leftarrow T_{fc} \end{array} \tag{17}$$

As an example, Sutherland's law can be applied to calculate the air thermal conductivity, as follows:

$$k_{\text{fluid}} = 2.495 \times 10^{-3} \left[T_{fc}^{1.5} \Big/ (T_{fc} + 194.0) \right] \tag{18}$$

Then, the fluid heat flux is given as

$$\boldsymbol{q}_{\text{fluid}} = -k_{\text{fluid}} \nabla T \tag{19}$$

At the solid side, the interface temperature T_{fc} can be calculated from the following relationship:

$$\boldsymbol{q}_{\text{solid}} \cdot \boldsymbol{n}_{fc} = -k_{\text{solid}} \frac{T_c - T_{fc}}{|\boldsymbol{r}_c - \boldsymbol{r}_{fc}|} \frac{\boldsymbol{r}_c - \boldsymbol{r}_{fc}}{|\boldsymbol{r}_c - \boldsymbol{r}_{fc}|} \cdot \boldsymbol{n}_{fc} = \boldsymbol{q}_{\text{fluid}} \cdot \boldsymbol{n}_{fc} \tag{20}$$

C. Cooling Channel Flow

For each cooling channel, the quasi-one-dimensional equations (5) are applied to (small) discrete channel segments (cells), and the values at the outlet are computed. Specifically, an iterative procedure can be applied to find pressure and enthalpy, which are selected to be the working variables, as follows:

$$V_2^{n+1,i} = \dot{m} \Big/ \left(\rho_2^{n+1,i} A_2 \right), \qquad \dot{m} = [(\rho V A)_1]^n \tag{21}$$

$$p_2^{n+1,i+1} = p_1^n - dp^{n+1,i} \tag{22}$$

$$h_2^{n+1,i+1} = \Delta Q^{n+1,i} + h_1^n + \tfrac{1}{2}\left[V_1^n\right]^2 - \tfrac{1}{2}\left[V_2^{n+1,i}\right]^2 + g(z_1 - z_2) \tag{23}$$

where i is an iteration counter. The pressure loss from inlet to outlet of each cooling cell results from viscous friction, velocity changes, and body force (gravity) and is given as follows:

$$\begin{aligned} dp^{n+1,i} = {} & (Lf/2)\left[\left(\rho_1^n + \rho_2^{n+1,i} \right) \Big/ 2 \right] \left[\left(V_1^n + V_2^{n+1,i} \right) \Big/ 2 \right]^2 \\ & \times [2/(D_1 + D_2)] + [2\dot{m}/(A_1 + A_2)] \left[V_2^{n+1,i} - V_1^n \right] \\ & + \left[\left(\rho_1^n + \rho_2^{n+1,i} \right) \Big/ 2 \right] g(z_2 - z_1) \end{aligned} \tag{24}$$

and the heat gain from the solid matrix is computed as follows:

$$\Delta Q^{n+1,i} = h_f^n \left\{ [T_{\text{wall,av}}]^n - \left[\left(T_1^n + T_2^{n+1,i} \right) \Big/ 2 \right] \right\} \tag{25}$$

where[21]

$$h_f = kNu/D, \qquad Nu = 0.023 Re^{0.8} Pr^{0.4}, \qquad Pr = c_p \mu / k \tag{26}$$

In Eq. (25), $T_{\text{wall,av}}$ is the average wall temperature of the cooling channel, and comes from the coupling with the solid matrix, to be discussed shortly.

Equations (22) and (23) can be solved iteratively, after initial values ($i = 0$) are given for pressure and specific enthalpy,

$$p_2^{n+1,i=0} = p_2^n, \qquad h_2^{n+1,i=0} = h_2^n \tag{27}$$

and using the thermodynamic model to recover values for density and temperature, as already mentioned.

Because the solid-phase temperatures change at each Newton iterative level, the computations for the cooling channel should be repeated at each Newton iteration. However, only a steady-state cooling channel model was implemented. Therefore, time accuracy was not a consideration. In this case, the cooling channel computations were scheduled once per time step.

D. Coupling Cooling Channels and Solid Matrix

The cooling channels are embedded within the solid matrix. However, the discretization of the solid matrix does not feature the channels explicitly. The coupling between the two models is based on the determination of the average wall temperature for each section of the cooling channel, as already mentioned. Solid matrix and cooling channels are discretized separately, and the coupling satisfies the energy conservation principle. This approach simplifies enormously the discretization of the solid matrix. The Loci framework allows the seamless transfer of information between the two models, which is necessary for a tight coupling of the numerical procedure.

More details on the coupling are provided next, for the case of a cooling channel with a circular cross section. A relationship between cooling channel and solid matrix is developed based on the energy conservation law, and is given as

$$\begin{aligned} 2\pi r q_{\text{solid}} &= 2\pi r_c q_{\text{cool}} \\ \Rightarrow r k_{\text{solid}} \frac{\mathrm{d}T}{\mathrm{d}r} &= r_c h_f (T_{\text{wall}} - T_{\text{cool}}) \\ \Rightarrow \mathrm{d}T &= \frac{r_c h_f (T_{\text{wall}} - T_{\text{cool}})}{r k_{\text{solid}}} \, \mathrm{d}r \end{aligned} \tag{28}$$

where q_{solid} is the heat flux in the solid, q_{cool} is the heat flux to the cooling channel wall, r is the distance between the centers of a solid cell and a cooling cell, r_c is the cooling channel radius, and T_{cool} is the mean temperature of the cooling channel segment.

Integrating Eq. (28) to recover the cooling channel temperature results in the following:

$$T_{\text{wall}} = \frac{(r_c h_f / k_{\text{solid}}) T_{\text{cool}} (\ell_n r - \ell_n r_c) + T_{\text{solid}}}{(r_c h_f / k_{\text{solid}})(\ell_n r - \ell_n r_c) + 1} \tag{29}$$

where T_{solid} is the temperature at a solid cell.

The average cooling channel wall temperature is computed as

$$T_{\text{wall,av}} = \frac{\oint T_{\text{wall}} \, \mathrm{d}l}{\oint \mathrm{d}l} \tag{30}$$

For the purpose of evaluating Eq. (30), a stencil of solid cells is constructed around the cooling cell, excluding the solid cells that contain the cooling cell.

IV. Numerical Results

The two heat transfer models introduced in this study have been extensively tested and validated. For details, refer to Liu.[27] In the following text two realistic engineering problems are simulated, and the numerical solutions are compared with available experimental data. The first case involves a fully coupled solid–fluid problem. The second case involves the coupling of all three models: fluid flow, solid matrix, and cooling channels.

A. Air in a Cooled Converging–Diverging Nozzle

The first test case is a fully coupled fluid–solid problem involving the flow of heated air in a cooled converging–diverging nozzle. The analysis of this case is based on the data reported by Back et al.[29] They investigated the convective heat transfer from turbulent boundary layers accelerated by large pressure gradients in a cooled converging–diverging nozzle. The test nozzle is axisymmetric, has a throat diameter of 0.0458 m, a contraction-area ratio of 7.75:1, an expansion-area ratio of 2.68:1, a convergent half-angle of 30 deg, and a divergent half-angle of 15 deg.

The nozzle meshes are shown in Fig. 1. The grid for the fluid region is composed of 150×79 cells, and the normal space from the first grid point to the nozzle wall is 1.0 μm. This corresponds to a y^+

Table 1 Operating parameters for nozzle flow

Parameters	Values
Inlet pressure, Pa	5.171×10^5
Inlet temperature, K	843.33
Inlet density, kg/m^3	2.1306
Transport model	Sutherland
Turbulence model	Spalart–Allmaras

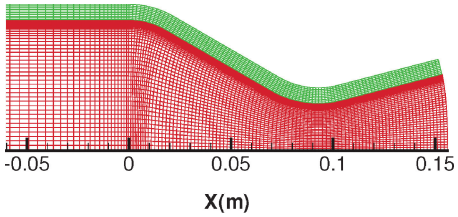

Fig. 1 Nozzle and solid wall meshes.

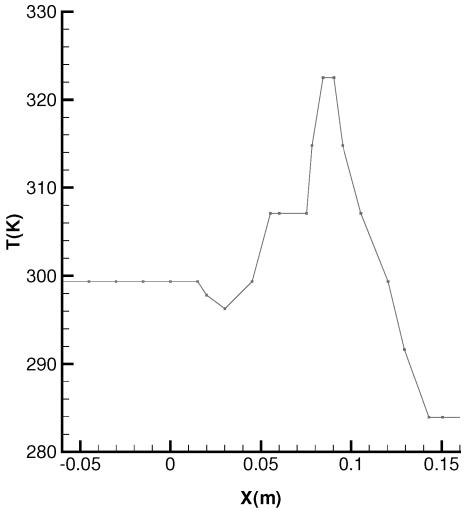

Fig. 2 Nozzle wall outside temperature.

ranging from approximately 0.13 at the inlet to approximately 0.50 at the oulet, based on the control volume thickness. Values based on the position of the control volume centroid would be approximately one-half of those mentioned. This is a fine grid for viscous calculations, and the numerical results obtained are grid independent. (A grid convergence study was conducted for the fluid region, featuring six meshes: three coarser grids, the current one, and two finer grids.) The solid region is discretized by means of 150×9 volumes, where the cells are matched in the longitudinal direction.

The computed domain matches the experimental one. The operating parameters for the fluid phase are listed in Table 1. All physical values are from the experimental apparatus[29]; more details on the numerical modeling can be found in Ref. 27. The following boundary conditions were employed: characteristic boundary conditions at the inlet and outlet (subsonic inflow and supersonic outflow), symmetry at the centerline, and no-slip for the interface. The temperature of the interface was computed by means of the coupling process with the solid matrix, as already discussed.

For the solid phase, the temperature at the external side of the nozzle wall was specified from experimental values and is shown in Fig. 2. The interface heat flux was extracted from the flow side, as already discussed. The temperatures at the solid sides that correspond to the nozzle inlet and outlet were specified as 299 and 283 K, respectively, as suggested by the experimental data. Computations were performed for three different American Iron and Steel Institute (AISI) stainless steels. The physical and thermal properties of the materials used are listed in Table 2 (Ref. 30). Because only the steady-state solution to this problem is of interest, independent time steps are chosen for the fluid mechanics and solid mechanics algorithms to accelerate convergence. A time step on the order of

Table 2 Physical and thermal properties of AISI stainless steels at 400 K

Material	Density, kg/m^3	Heat capacity, J/(kg · K)	Thermal conductivity, W/(m · K)
AISI302	8055	512	17.3
AISI304	7900	515	16.6
AISI316	8238	504	15.2

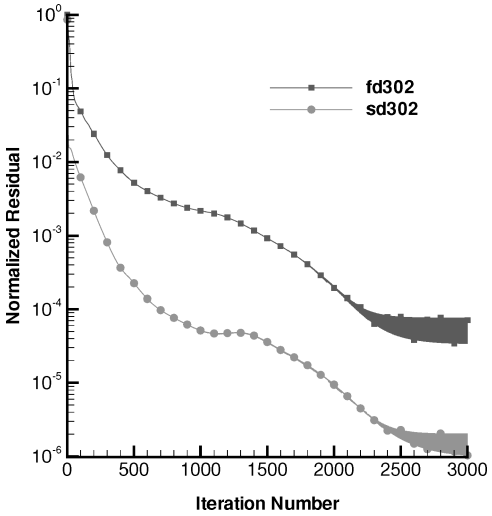

Fig. 3 Convergence history for solid and flow solvers.

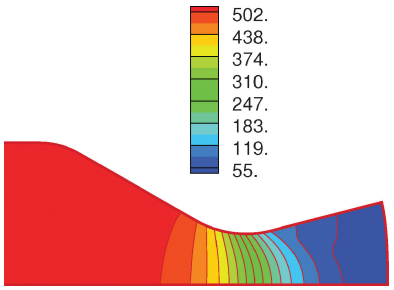

Fig. 4 Nozzle flow pressure (kiloPascals).

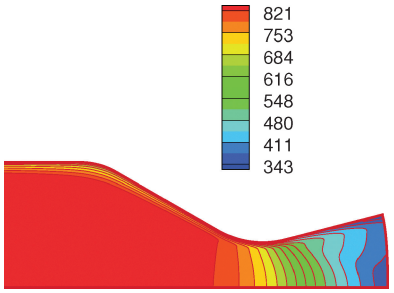

Fig. 5 Nozzle flow temperature (Kelvin).

seconds is used for the solid part, whereas the fluid part time step is on the order of milliseconds.

The coupled convergence history is shown in Fig. 3, where the label fd302 stands for fluid coupled with an AISI302 solid, and sd302 stands for an AISI302 solid. Note that a four order of magnitude reduction in residuals for both the solid and gas phases is achieved. Similar results apply to the other kinds of steel.

The nozzle flow pressures, temperatures, and Mach numbers are shown in Figs. 4, 5, and 6, respectively. Solid wall temperature contours are shown in Fig. 7, and coupled temperature contour slices are shown in Fig. 8.

A comparison of the computed heat transfer coefficient with experimental results provided by Back is shown in Fig. 9. The heat transfer coefficient is defined as the ratio between heat flux and

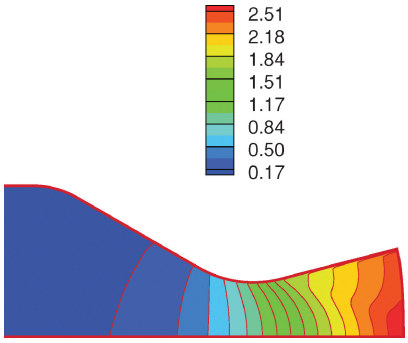

Fig. 6 Nozzle flow Mach number.

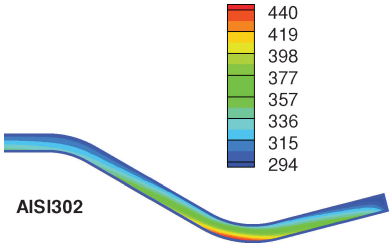

Fig. 7 Solid wall temperature (Kelvin).

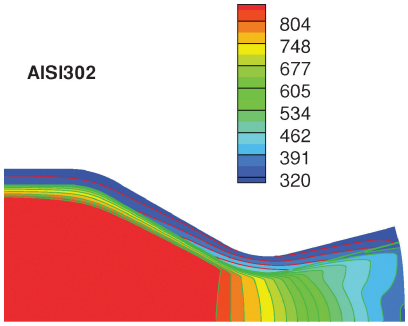

Fig. 8 Nozzle flow and solid wall temperature (Kelvin).

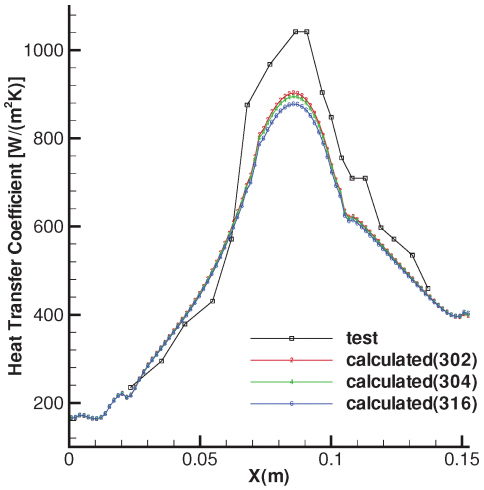

Fig. 9 Comparison of wall heat transfer coefficients.

temperature difference (adiabatic minus wall temperatures). The comparison is satisfactory. However, results that are even more promising are the computed wall temperatures, shown in Fig. 10. Figure 10 shows the predicted wall temperatures from an earlier uncoupled case and from the current coupled case. The experimental results are also included under the label "test." Note that the temperature predictions are significantly improved by the coupling of fluid- and solid-phase simulations. Moreover, the predicted wall temperatures are very close to the experimental values. Similar results apply for the other two kinds of steel that were investigated.

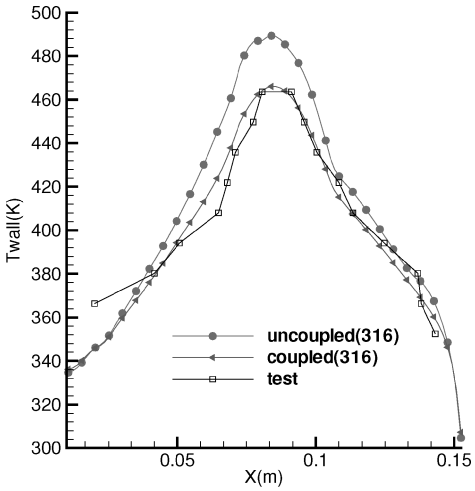

Fig. 10 Comparison of wall temperatures.

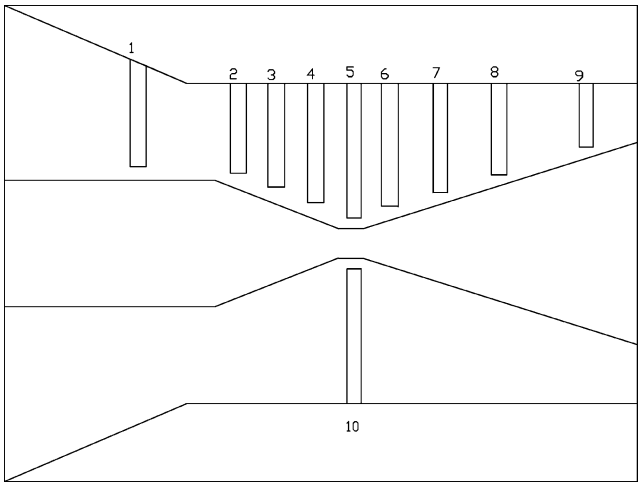

Fig. 11 Nozzle section and thermocouple locations.

B. RBCC Thruster Nozzle Simulation

A more complex computation was carried out for an RBCC thruster nozzle. This analysis is based on the experimental data reported by Pal et al.[10] Heat transfer characteristics were investigated, particularly at the throat, where the peak heat flux occurs. This thruster has a two-dimensional section, and the geometry is very compact, as required by packaging considerations. A schematic of the nozzle is shown in Fig. 11. The nozzle itself has a length of 50.8 mm, a height of 44.45 mm, and a width of 76.2 mm. The nozzle throat height is small (2.5 mm), and the outlet height is 15.24 mm. GO_2 and GH_2 are used. The design includes two oxygen-free high-conductivity copper sections welded together to make up the nozzle flowpath, with stainless steel plates welded at the top and bottom to strengthen the structure. The numbers ranging from 1 to 10 shown in Fig. 11 denote each thermocouple hole. The type-K thermocouples are silver brazed to the bottom of the holes, with approximately 1.27 mm of material separating them from the hot gases. Thermocouples 3 and 10 were not used. The remaining eight thermocouples were employed to obtain the experimental data.[10]

Both the chamber and nozzle of the thruster are fully water cooled. The nozzle is cooled on all four sides. The water cooling passages have a diameter of 1.5875 mm and run parallel to the inside nozzle walls. There are 24 channels positioned in each of the top and bottom walls, and four are in each side wall. The cooling channel passages in the top nozzle wall are shown in Fig. 12. Water enters from the center manifolds, provides impingement cooling to the throat region, bifurcates to cool the converging and diverging sections, then exits through two manifolds. There are four identical independent water circuits (two each on top and bottom) that are separated by a

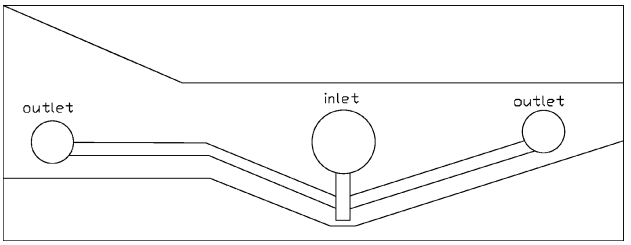

Fig. 12 Cooling channel passages in the top nozzle wall.

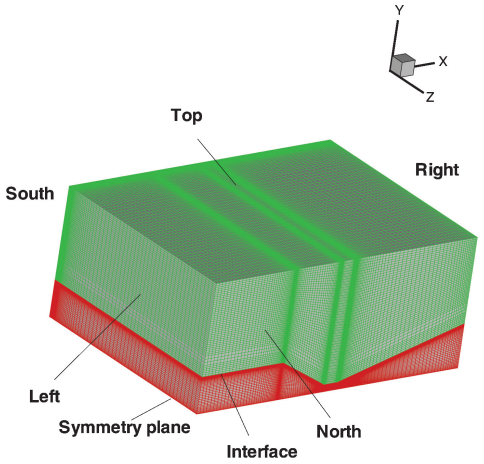

Fig. 13 Thruster fluid and solid grids.

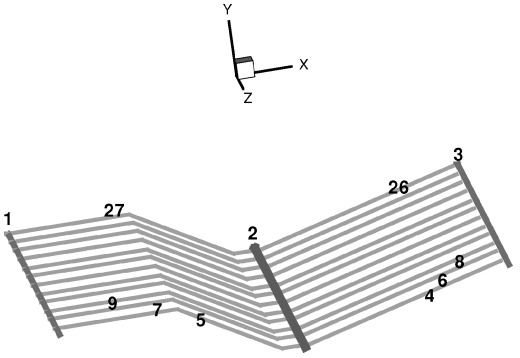

Fig. 14 Cooling lines arrangement.

2.54-mm middle land region on the top and bottom walls, where the type-K thermocouples are located. The thermocouple temperatures and water inlet and outlet temperatures were recorded during the experiment.

The cooling channel passages are formed by drilling and sealing processes, and so the actual design of the nozzle wall is very complex. Therefore, a simplified geometric model was utilized to reduce the grid generation difficulties and computational cost of the simulation. The computational meshes for both the nozzle flow and wall are shown in Fig. 13, which is one-fourth of the whole geometry due to symmetry. (The nozzle side is not shown.) The grid for the fluid region is composed of $161 \times 54 \times 90$ volumes, and the normal distance from the first grid point to the nozzle wall is 1.0 μm. This corresponds to an estimated maximum value of y^+ of approximately 0.6, based on the thickness of the control volume. The grid for the solid region features the same number of volumes ($161 \times 54 \times 90$); moreover, the cells at the interface are matched.

The cooling channel arrangement is shown in Fig. 14. In the computational domain, there are 12 channels cooling each of the converging and diverging portions of the nozzle wall, plus 3 main horizontal channels, for a total of 27 channels, as indicated in Fig. 14. Water enters from the second (2) central channel, bifurcates to channels 4 and 5, 6 and 7, . . . , 26 and 27, then exits from channels 1 and 3.

Table 3 Inflow conditions and computational model

Parameters	Values
O/F ratio	8.0
Inlet pressure, Pa	3.4476×10^6
Inlet temperature, K	3576
Inlet density, kg/m^3	1.8158
H_2 inflow rate, kg/s	0.034473
O_2 inflow rate, kg/s	0.2758
Specific heat ratio	1.1282
Molecular Weight	15.642
Sound speed, ms	1464.4
Mass Fractions	
H	0.002744
H_2	0.01657
H_2O	0.75654
O	0.02115
OH	0.11824
O_2	0.08477
Chemistry model	Finite rate
Turbulence model	Menter's BSL

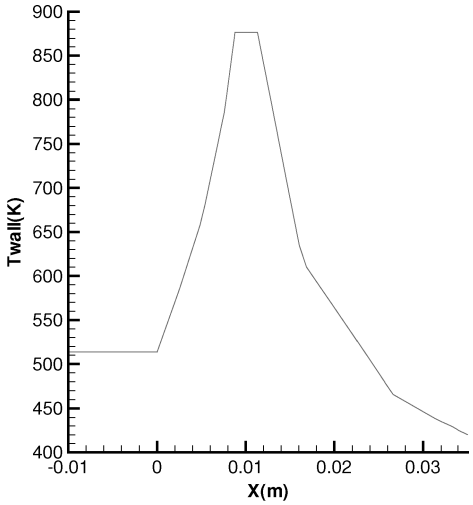

Fig. 15 Specified side wall temperature.

The boundary conditions employed for the fluid domain are summarized in the following text. The inflow boundary was partially determined by the mass flow rate specified in the experiments. The fuel and oxidizer were assumed to be completely mixed and in chemical equilibrium. The equilibrium properties at the experimental chamber pressure and mixture ratio were obtained using CEA[31] and are summarized in Table 3. Case 12 of the experimental sequence was employed.[10] The outflow boundary was treated as a supersonic outflow, whereby all variables are extrapolated from the interior of the domain. The interface featured a no-slip boundary condition, and its temperature was computed by the coupling process. The north side wall boundary was specified by symmetry considerations. The south side wall temperature was set to vary in the axial direction, according to the profile shown in Fig. 15, which was derived from the two-dimensional calculations reported by Pal et al.[10] One more symmetry plane completes the description of the fluid region boundaries (Fig. 13).

For the solid matrix, the operating parameters and boundary conditions are listed in Table 4. The interface heat flux was extracted from the nozzle flow, as already discussed. The constant values of temperature for south, left, right, and top walls were specified as an approximation of the experimental data. Temperature-dependent properties were used in the solid matrix, with coefficients obtained by fitting available data.[30]

The cooling channels inlet conditions are listed in Table 5. Currently, the cooling channel model can allow multiple, independent lines, but line crossing is not modeled. Therefore, each channel needs an individual inlet condition. All channels were assumed to be smooth. The inlet temperature and mass flow rate set for channel 2

Table 4 Operating parameters for thruster nozzle wall

Boundary conditions	Values
South, K	300
Bottom	interface
Left, K	400
North	symmetry
Top, K	350
Right, K	350
Physical properties	
Heat capacity, J/(kg K)	$355.6(1+2.8\times10^{-4}T)$
Thermal conductivity, W/(m K)	$419.8(1-1.6\times10^{-4}T)$
Density, kg/m^3	8933

Table 5 Cooling channel inlet conditions

Channel index	Values
Inlet temperature, K	
1	304
2	287
3	302
4–27	287
Inlet pressure, kPa	
1	477
2	500
3	481
4–27	500
Inlet mass flow rate, kg/s	
1	0.2518
2	0.5036
3	0.2518
4–27	0.02098
Channel radius, m	
1	0.002286
2	0.003556
3	0.002286
4–27	0.0007937

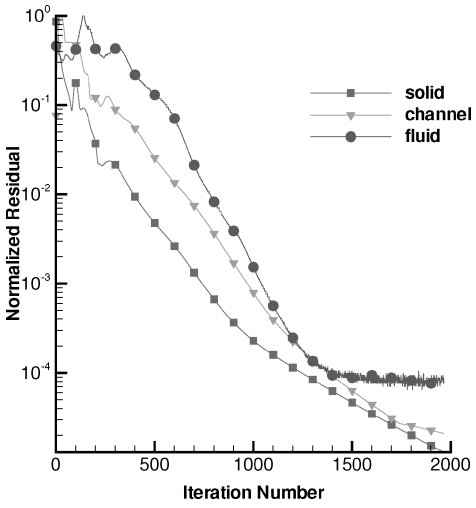

Fig. 16 Residual history for fluid, solid, and channel calculations.

were taken from the experiment, the pressure was initially set as 500 kPa; inlet temperatures for channels 4–27 were specified to be the same as channel 2, assuming changes along channel 2 are small; conditions specified for channel 1 and 3 were obtained from an early two-dimensional calculation. Specifically, in the two-dimensional model, just two channels were present: from the throat to the converging and diverging sections, respectively. Their inlet conditions were specified to be the same as channel 4. All other conditions were kept unchanged. The outlet data obtained are now used as the inlet condition for channels 1 and 3 in the current three-dimensional analysis.

The residual history for this calculation is shown in Fig. 16. A four-order of magnitude reduction in residuals for nozzle flow, solid

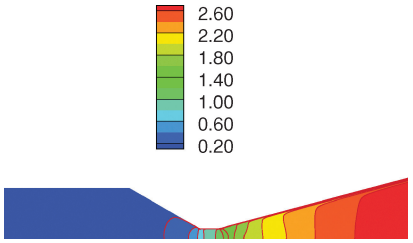

Fig. 17 Flow Mach number distribution.

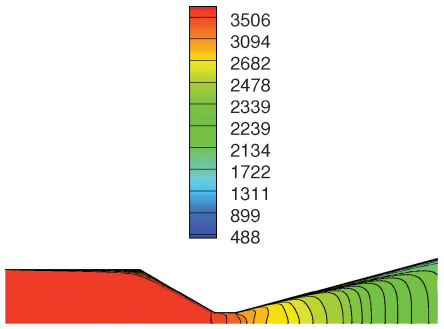

Fig. 18 Flow temperature distribution (Kelvin).

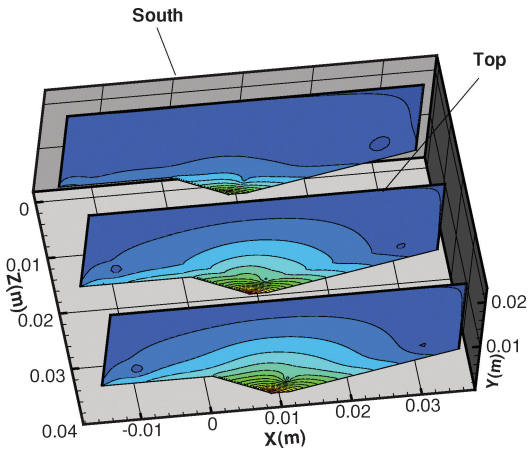

Fig. 19 Temperature contour slices: solid wall.

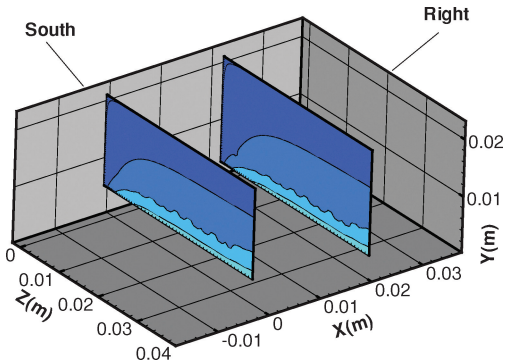

Fig. 20 Temperature contour slices: solid wall.

heat transfer, and cooling channel calculations is achieved. The nozzle flow Mach number and temperature are shown in Figs. 17 and 18, respectively. The results suggest that the flow is well behaved because no recirculation around the sharp corner was found. The Mach number at the exit plane is 2.808, and the temperature drops from 3579 to 2174 K.

A sample of temperature contours in the solid phase is shown in Figs. 19 and 20. The cooling channel path is explicitly shown in

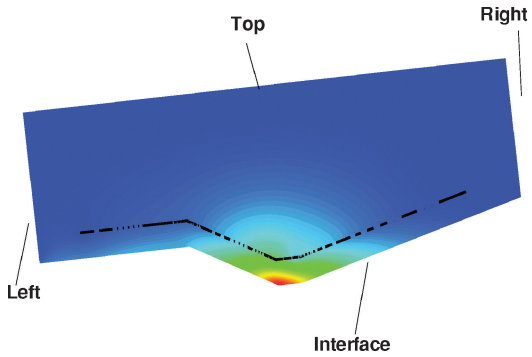

Fig. 21 Solid-phase temperature: cooling path shown.

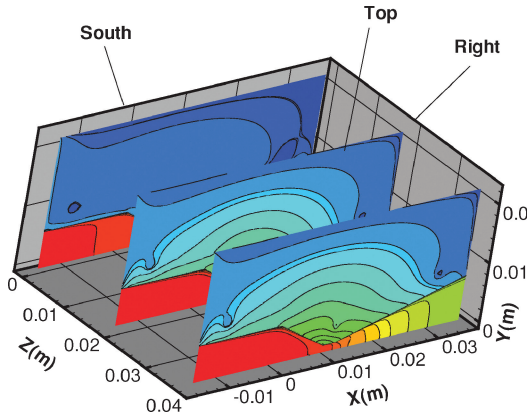

Fig. 22 Nozzle and solid wall temperature contour slices.

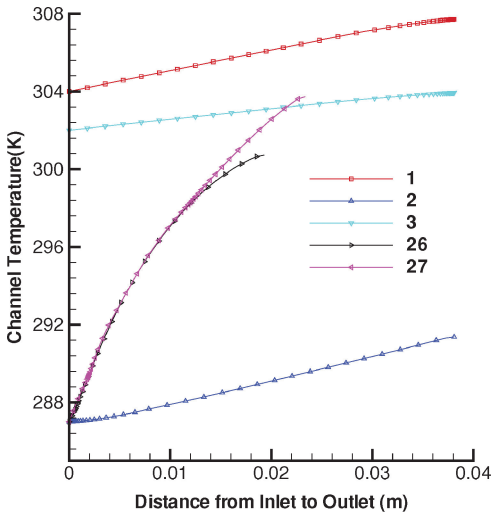

Fig. 23 Cooling channel temperatures.

Fig. 21. Both nozzle flow and solid wall temperatures are shown in Fig. 22. The cooling effects are evident in the local temperature contours, which proves that the cooling channels are working well.

The cooling channel temperature along the flow direction is shown in Fig. 23. The temperature difference between inlet and outlet is shown in Fig. 24. The temperature changes in the channel lines for the converging and diverging sections of the nozzle are higher than those for the side walls. Moreover, using the outlet values of channels 26 and 25 as the inlet conditions for channels 1 and 3 is shown to be acceptable. The outlet temperatures are compared with the experimental data in Table 6. The maximum discrepancy is approximately 2.8%.

The computed nozzle wall heat flux is given in Fig. 25. The heat flux peaks at the nozzle throat, due mostly to the sharp corners in the

Table 6 Cooling channel outflow temperatures

Channel index	Calculated outflow T, K	Measured outflow T, K
1	307.7	316.33
3	303.939	308.63

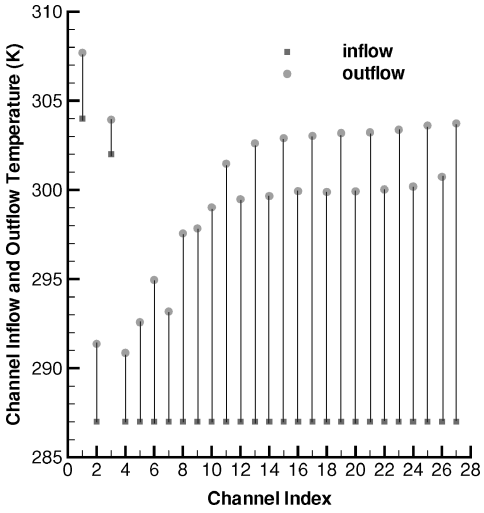

Fig. 24 Cooling channel inflow and outflow temperatures.

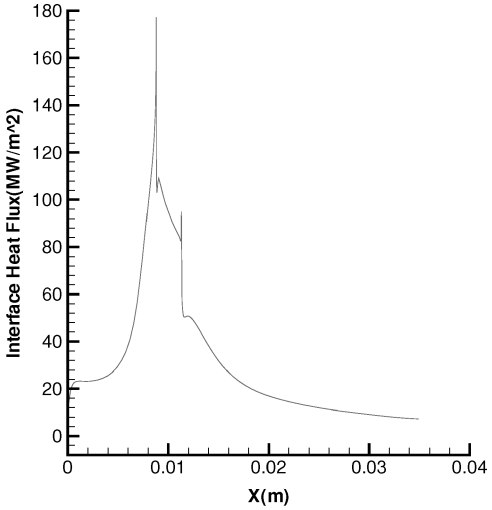

Fig. 25 Interface heat flux.

nozzle profile and the flow acceleration. The computational results are higher than previously reported results,[10] which were obtained from a combination of a one-dimensional analytical model and two-dimensional numerical predictions. The computed wall temperature is shown in Fig. 26, and the temperatures at the thermocouple positions are shown in Fig. 27, together with the measured results. The computed temperatures at the thermocouple locations are higher than the experimental data. The discrepancy is probably due to the differences between the real and modeled geometries of the nozzle. As already mentioned, the cooling passages were formed by first drilling, then sealing at the appropriate place to match the dimension requirements. Holes for burying thermocouples were drilled on the top and bottom nozzle walls. The resulting nozzle structure was fully three dimensional. The byproducts of machining and the channels in the side walls were not considered in this study, due to the difficulties of generating a grid for such a geometry. It is likely that the instrumented nozzle wall was cooled more than the computational model. A more complete simulation of the instrumented nozzle requires more work on grid generation and probably a generalized grid.[28]

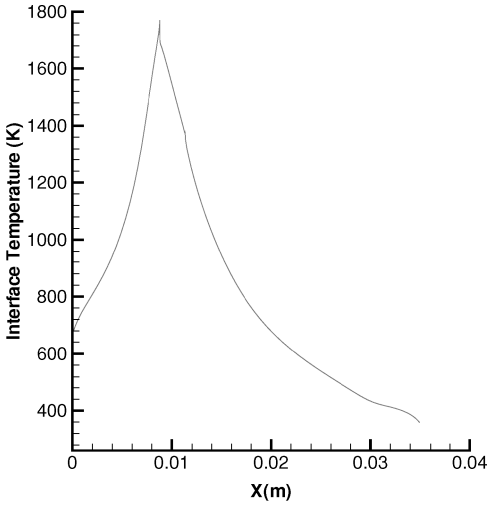

Fig. 26 Interface temperature.

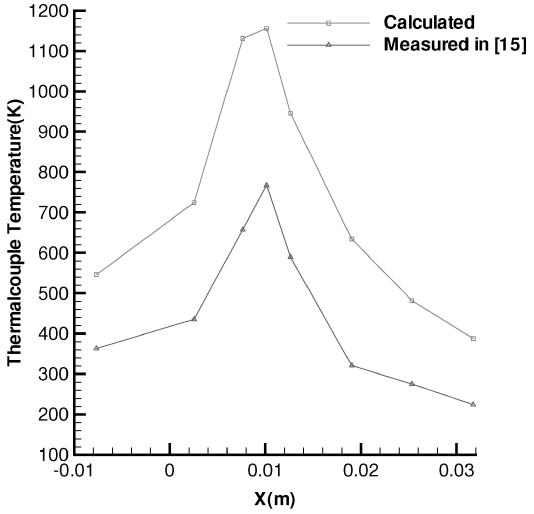

Fig. 27 Thermocouple temperatures.

Overall, the simulations provided reasonable results that validate the models developed and implemented. Moreover, the ability to tackle realistic engineering applications was demonstrated.

V. Conclusions

The present study was focused on the coupling of three different physical models, all of which are necessary for the accurate simulation of heat transfer problems in propulsion systems. By the use of a flexible application framework to reduce the complexitity of assembling disparate algorithms, the three models were fully coupled. Results from two test cases were presented, and compared well with available experimental data. The RBCC thruster nozzle test case was very challenging from a geometrical point of view, requiring some simplifications to be made. However, a reasonably representative model was developed, and the results obtained are very encouraging.

Coupling the cooling channel flow model with the solid-phase heat transfer and fluid dynamic models provides a good starting point for further extensions to more complex physical models, such as the inclusion of thermal stress analysis, or the introduction of composite materials. Whereas the results of this study look quite promising, there is much left to address. Cooling channel networks can be very complex, and the channels might cross each other. In such cases, the simplifications adopted in the model would have to be carefully reexamined, and the grid generation strategy would become significantly more difficult. Fully coupling physical models from several disciplines and spatial domains will require further enhancements in both physical modeling and grid generation technology.

Acknowledgments

The Department of Aerospace Engineering at Mississippi State University partially supported the first author, and NASA Marshall Flight Research Center partially supported all of the authors, with Jeffrey S. West serving as a very enthusiastic, spirited, and encouraging Technical Monitor. The authors would like to thank Lin Tang, Senior Research Associate (retired) with the SimCenter at Mississippi State University for his invaluable help in this effort. He performed the grid resolution study for the first test case and helped with the bibliographical research. Additionally, Xiao-Ling Tong, Research Assistant Professor at the SimCenter, Junxiao Wu, Research Assistant Professor at the Center for Advanced Vehicular Systems, and Thomas George, Research Associate at the SimCenter, were willing and able to lend a helping hand when needed.

References

[1]Shope, F. L., "Conjugate Conduction–Convection Heat Transfer with a High-Speed Boundary Layer," *Journal of Thermophysics and Heat Transfer*, Vol. 8, No. 2, 1994, pp. 275–281.

[2]DeLise, J. C., and Naraghi, M. H. N., "Comparative Studies of Convective Heat Transfer Models for Rocket Engines," AIAA Paper 95-2499, July 1995.

[3]Janus, J. M., and Newman, J. C., "Aerodynamic and Thermal Design Optimization for Turbine Airfoils," AIAA Paper 2000-0840, Jan. 2000.

[4]Sondak, D. L., and Dorney, D. J., "Simulation of Coupled Unsteady Flow and Heat Conduction in a Turbine Stage," *Journal of Propulsion and Power*, Vol. 16, No. 6, 2000, pp. 1141–1148.

[5]Webster, R. S., "A Numerical Study of the Conjugate Conduction–Convection Heat Transfer Problem," Ph.D. Dissertation, Dept. of Aerospace Engineering, Mississippi State Univ., Mississippi State, MS, May 2001.

[6]Naraghi, M. H. N., "RTE—A Computer Code for Three-Dimensional Rocket Thermal Evaluation," Ver. 1, Tara Technologies, LLC, Yorktown Heights, NY, Jan. 2002.

[7]Nickerson, G. R., and Coats, D. E., and Dang, A. L., and Dunn, S. S., and Kehtarnavaz, H., "Two-Dimensional Kinetics (TDK) Nozzle Performance Computer Program," NASA Advanced Supercomputing, Rept. 836863, March 1989.

[8]Hendricks, R. C., and Peller, I. C., and Baron, A. K., "WASP–A Flexible Fortran IV Computer Code for Calculating Water and Steam Properties," NASA TN D-7391, Nov. 1973.

[9]Hendricks, R. C., and Baron, A. K., and Peller, I. C., "GASP–A Computer Code for Calculating the Thermodynamic and Transport Properties for Ten Fluids: Parahydrogen, Helium, Neon, Methane, Nitrogen, Carbon Monoxide, Oxygen, Fluorine, Argon, and Carbon Dioxide," NASA TN D-7808, Feb. 1975.

[10]Pal, S., and Tucker, K., and Lehman, M., and Santoro, R. J., "Experimental Studies of Heat Transfer in Rectangular Nozzles for CFD Design Methodology," *Proceedings of the 33rd ASME/AIChE/ANS/AIAA National Heat Transfer Conference*, AIAA, Reston, VA, 1999, pp. 168–177.

[11]Chen, Y. S., "Compressible and Incompressible Flow Computations with a Pressure Based Method," AIAA Paper 89-0286, Jan. 1989.

[12]Bartz, D. R., "A Simple Equation for Rapid Estimation of Rocket Nozzle Convective Heat Transfer Coefficients," *Jet Propulsion*, Vol. 27, Jan. 1957, pp. 49–51.

[13]Bartz, D. R., "Turbulent Boundary-Layer Heat Transfer from Rapidly Accelerating Flow of Rocket Combustion Gases and of Hot Air," *Advances in Heat Transfer*, Vol. 2, No. 3, 1965, pp. 2–108.

[14]Luke, E. A., "A Rule-Based Specification System for Computational Fluid Dynamics," Ph.D. Dissertation, Mississippi State Univ., Mississippi State, MS, Dec. 1999.

[15]Cinnella, P., and Grossman, B., "Computational Methods for Chemically Reacting Flows," *Handbook of Fluid Dynamics and Fluid Machinery*, Wiley, New York, 1996, pp. 1541–1590.

[16]Tong, X.-L., Luke, E. A., and Cinnella, P., "Numerical Simulations of Chemically Reactive Turbulent Flows Using the Loci System," *Proceedings of the SECTAM-XX Conference*, FM-19, Auburn Univ., College of Engineering, Auburn, AL, 2000, pp. 166–173.

[17]Wu, J. X., Tang, L., Tong, X.-L., Luke, E., and Cinnella, P., "Comprehensive Numerical Study of Jet Flow Impingement over Flat Plates at Varied Angles," *Journal of Spacecraft and Rockets*, Vol. 39, No. 3, 2001, pp. 357–366.

[18]Luke, E. A., Tong, X.-L., Wu, J., Tang, L., and Cinnella, P., "A Step Towards 'Shape-Shifting' Algorithms: Reactive Flow Simulations Using Generalized Grids," AIAA Paper 2001-0897, Jan. 2001.

[19]Spalart, P., and Allmaras, S. R., "A One-Equation Turbulence Model for Aerodyanamic Flows," *Aerospace Science and Technology*, Jan. 1994, pp. 5–22.

[20]Menter, F. R., "Two-Equation Eddy–Viscosity Turbulence Models for Engineering Applications," *AIAA Journal*, Vol. 32, No. 8, 1994, pp. 1598–1605.

[21]Kakac, S., and Yener, Y., *Convective Heat Transfer*, 2nd ed., CRC Press, Boca Raton, FL, 1994, p. 131.

[22]Colebrook, C. F., "Turbulent Flow in Pipes with Particular Reference to the Transition Region Between the Smooth and Rough Pipe Laws," *Journal of Institute of Civil Engineers*, Vol. 11, Feb. 1939, pp. 133–156.

[23]Chen, N. H., "An Explicit Equation for Friction Factor in Pipe," *Industrial and Engineering Chemistry Fundamentals*, Vol. 18, No. 3, 1979, pp. 296, 297.

[24]International Association for the Properties of Water and Steam, "Release on the IAPWS Formulation 1995 for the Thermodynamic Properties of Ordinary Water Substance for General and Scientific Use," Fredericia, Denmark, Sept. 1996.

[25]International Association for the Properties of Water and Steam, "Revised Release on the IAPWS Formulation 1985 for the Viscosity of Ordinary Water Substance," Erlangen, Germany, Sept. 1997.

[26]International Association for the Properties of Water and Steam, "Release on the IAPWS Formulation 1985 for the Thermal Conductivity of Ordinary Water Substance," London, Sept. 1988.

[27]Liu, Q. Y., "Coupling Heat Transfer and Fluid Flow Solvers for Multi-Disciplinary Simulations," Ph.D., Dissertation, Dept. of Aerospace Engineering, Mississippi State Univ., Mississippi State, MS, Aug. 2003.

[28]Koomullil, R., and Soni, B., "Flow Simulation Using Generalized Static and Dynamic Grids," *AIAA Journal*, Vol. 37, No. 12, 1999, pp. 1551–1557.

[29]Back, L. H., Massier, P. F., and Gier, H. L., "Convective Heat Transfer in a Converging–Diverging Nozzle," *International Journal of Heat Mass Transfer*, Vol. 7, May 1964, pp. 549–568.

[30]Incropera, F. P., and DeWitt, D. P., *Introduction to Heat Transfer*, Wiley, New York, 1990.

[31]McBride, B. J., and Gordon, S., "Computer Program for Calculation of Complex Equilibrium Compositions and Applications," NASA Reference Publication 1311, June 1996.